Electrolytic Micro-Capacitors Based on Tantalum Films for High Voltage Applications

Cédric Teyssedou, Jérémie Chaillou, Isabelle Roch-Jeune, David Troadec, Marielle Huvé, Pascal Roussel, Christophe Lethien

ADVANCED MATERIALS TECHNOLOGIES
www.advmattechnol.de

Electrolytic Micro-Capacitors Based on Tantalum Films for High Voltage Applications

Cédric Teyssedou, Jérémie Chaillou, Isabelle Roch-Jeune, David Troadec, Marielle Huvé, Pascal Roussel, and Christophe Lethien**

Electrolytic capacitors are known to be fast devices with very low time constant and able to deliver high power. This class of capacitors is then an interesting technology to power miniaturized embedded electronics for Internet of Things applications. However, the current electrolytic capacitor suffers from its bulky size that does not fit with the miniaturization. To solve this issue, a proof-of-concept consisting of miniaturizing an electrolytic capacitor based on tantalum materials to give rise to a new class of electrolytic micro-capacitors is proposed. To reach this ambitious objective, thin films (<100 nm) of tantalum metal (Ta), tantalum nitride (TaN), and tantalum oxide (Ta_2O_5) are deposited on a Si substrate by sputtering deposition method. After a careful optimization of the deposition parameters, Ta/Ta_2O_5 and TaN/Ta_2O_5 electrodes (Ta and TaN ≈45 nm and Ta_2O_5 ≈25 nm) and study their behaviors when biased at high voltage (>20 Volts) in aqueous electrolyte are produced. The Ta/Ta_2O_5 and TaN/Ta_2O_5 interfaces when the electrode is polarized near and beyond the breakdown voltage of the dielectric layer are carefully investigated. Polarizing the electrodes beyond the breakdown voltage are shown to result in anodization-like mechanisms. In the case of the TaN/Ta_2O_5 electrode, an N-rich porous layer grew within the Ta_2O_5 layer as polarization increased. A comparative study on the 2 stacked layers electrodes with different compositions (Ta/Ta_2O_5 and TaN/Ta_2O_5) but similar thicknesses (45/25 nm) is carried out: both electrodes show excellent capacitance retention of over 90% over 300 000 cycles. The frequency behavior of Ta/Ta_2O_5 and TaN/Ta_2O_5 electrodes shows that both are potential candidates in electrolytic micro-capacitors for powering miniaturized electronics.

1. Introduction

Advances in the miniaturization of electronic components have enabled the development of the Internet of Things (IoT). The miniaturized IoT consists of a multitude of electronic microdevices that can, for example, collect and transmit data, or be remotely controlled via network infrastructures.[1,2] A large number of applications stem from this concept, such as the possibility of carrying out remote maintenance, implanting sensors in the human body to monitor the evolution of a disease, tracking animals for migration purposes, or monitoring a forest to warn of a fire as quickly as possible.[3–5] However, as these small-footprint surface devices are autonomous, and thus not connected to the grid, they require miniaturized Electrochemical Energy Storage (EES) powered by micro-generators that use solar, thermal, mechanical, and electromagnetic energy to charge the small EES.[6] One of the most widely studied solutions for powering autonomous micro-devices is the triboelectric nanogenerator (TENG), which harvests mechanical energy issued

C. Teyssedou, J. Chaillou, I. Roch-Jeune, D. Troadec, C. Lethien
Institut d'Electronique
de Microélectronique et de Nanotechnologies
Université de Lille
CNRS
Université Polytechnique Hauts-de-France
UMR 8520 – IEMN, Lille F-59000, France
E-mail: christophe.lethien@univ-lille.fr

The ORCID identification number(s) for the author(s) of this article can be found under https://doi.org/10.1002/admt.202400682

DOI: 10.1002/admt.202400682

C. Teyssedou, J. Chaillou, C. Lethien
Réseau sur le Stockage Electrochimique de l'Energie (RS2E)
CNRS FR 3459, 33 rue Saint Leu, Amiens 80039, France

C. Teyssedou, M. Huvé, P. Roussel
Unité de Catalyse et de Chimie du Solide (UCCS)
Université de Lille
CNRS
Centrale Lille
Université d'Artois
UMR 8181 – UCCS, Lille F-59000, France
E-mail: pascal.roussel@univ-lille.fr

C. Lethien
Institut Universitaire de France (IUF)
Saint-Michel 103, Paris 75005, France

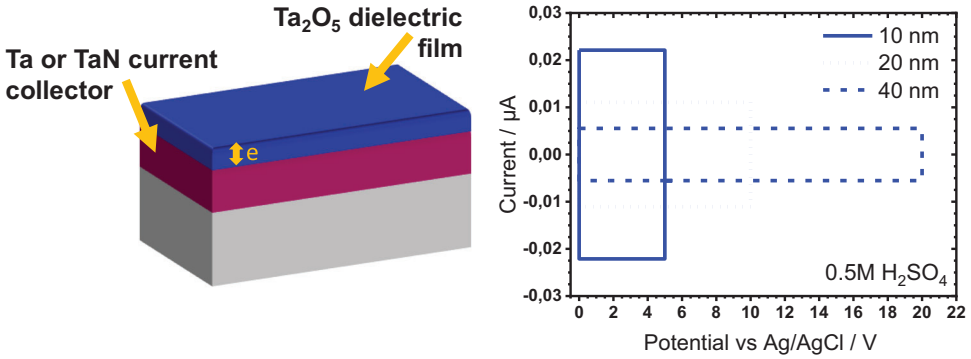

Figure 1. Schematic diagram of thin film electrodes for a miniaturized electrolytic capacitor. The 3 graphs represent theoretical rectangular shape cyclic voltammetry plots in 0.5 M H_2SO_4 electrolyte for Ta/Ta_2O_5 or TaN/Ta_2O_5 electrodes with various Ta_2O_5 thicknesses, from 10, 20, and 40 nm respectively.

from the environment and converts into a current pulse with a frequency ranging from a few tens to a few hundreds of hertz.[6] However, a device is needed to transform the alternating current (AC) from the TENGs into a direct current (DC) to charge the micro-storage devices. In addition, a micro-device integrated into the IoT must be able to transmit the data it has collected, and wireless data transmission requires considerable electrical power.[7] Two types of devices can address the issues discussed above, i.e., converting AC voltage to DC and providing sufficient power to transmit data as fast as possible. The first is the Electrolytic Capacitor (EC), formed by anodizing a tantalum or an aluminum metal film resulting in the growth of a barrier dielectric film that develops a large specific surface area.[8] These devices retain most of their capacity when loaded at several hundred hertz[8] and are also known to deliver high power thanks to their wide potential window, determined by the breakdown voltage of their barrier dielectric layer (from 2 to 630 V).[9] However, most of these devices are currently too cumbersome to be integrated into miniaturized electronic devices. The second type of device that can address both issues is Micro-Supercapacitors (MSCs). There are two main types of MSC: electrochemical double-layer capacitors (EDLC), which are mainly porous carbon-based materials that develop a very large specific surface area and store energy via the adsorption of a very large number of ions at the electrode/electrolyte interface.[10] The second major family of MSCs is based on pseudocapacitive materials, which store energy via fast and reversible redox surface reactions at the electrode/electrolyte interface. These devices are however limited by the electrochemical stability of the used electrolyte (<4 V).[7,11] To achieve power levels equivalent to those of ECs, MSCs have to be connected in series, but this approach reduces the surface capacitance and enlarges the footprint surface which is useless from a miniaturization point of view. The risk of failure is then increased, since if one MSC fails, the MSCs in series configuration fail.[12]

In the present manuscript, the alternative route of miniaturizing an electrolytic capacitor to make it suitable for integration as an electrolytic micro-capacitor was explored. We focus on tantalum-based technology since Ta_2O_5 is widely used in bulk electrolytic capacitors taking benefit from the high dielectric constant of Ta_2O_5 to maximize the specific capacitance.[9] The fabrication of electrolytic micro-capacitors and more specifically the deposition of tantalum metal, tantalum nitride, and tantalum oxide films will be achieved by thin-film deposition technique compatible with the microelectronics industry, enabling rapid integration and upscaling should the technology become relevant.[7] The selected sputtering deposition method gives us precise control over the composition, morphology, and thickness of the stacked layers on Si substrate. Two sputtered electrodes based on Ta_2O_5 dielectric film were investigated using various current collectors: Si/Ta/Ta_2O_5 and Si/TaN/Ta_2O_5. The Ta/Ta_2O_5 stacked layers are widely used as an anode in bulk electrolytic capacitors[5,9] unlike the Si/TaN/Ta_2O_5 electrode.

Figure 1 shows a schematic diagram of miniaturized electrolytic capacitor anodes in which three theoretical rectangular cyclic voltammetry in aqueous electrolytes are represented. These CV plots correspond to the shape of a purely capacitive electrode made from Ta_2O_5 dielectric layer with various thicknesses from 10 to 40 nm and clearly highlight the compromise between the expected capacitance and the accessible cell voltage. Due to the presence of the dielectric barrier, the electrochemical water splitting reaction could be avoided while the thermodynamic potential is close to 1.23 V at 25 °C and 1 atm, thus preventing the micro-devices from gas generation at high voltage.[13,14] As expected, the cell voltage is thus significantly enhanced but in that case, it is important to take into account the breakdown voltage of the dielectric layer to avoid film degradation and failures inside the micro-capacitor.

The electrode's capacitance (in Farad/F) is purely electrostatic, so it can be expressed by Equation (1), with ϵ_o vacuum permittivity, ϵ_r the dielectric constant of the material, S electrode surface and e the thickness of the dielectric barrier layer. The potential window is related to the breakdown voltage, V_{bd} (in Volt/V) of the dielectric barrier layer, which can be expressed as the product of the breakdown field E_{bd} (in Volt per meter/V m^{-1}) and the thickness of the dielectric film (see Equation (2)). The amount of energy (in Joule/J) that can be stored by the electrode is expressed by Equation (3). From Equations (1) and (2), it is clear that the dielectric layer plays an important role in the micro-capacitor as well as the metal/dielectric interface.

$$C = \frac{\varepsilon_o \times \varepsilon_r \times S}{e}, \text{ in Farad} \quad (1)$$

$$V_{bd} = E_{bd} \times e, \text{ in Volt} \quad (2)$$

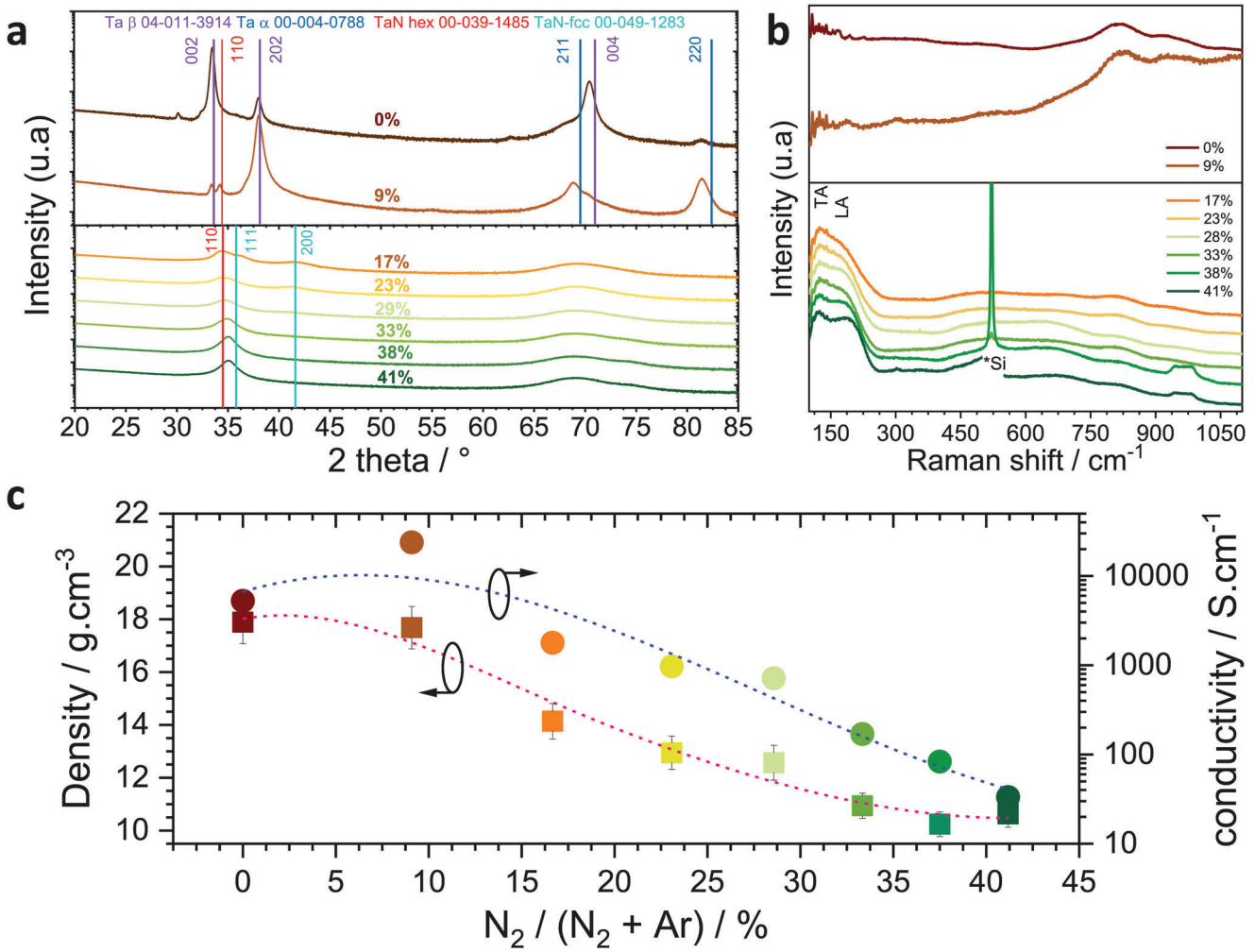

Figure 2. Effect of nitrogen flow rate within the plasma during the reactive deposition process of TaN films. a) XRD analyses of thin films obtained at different flow rates. b) Raman spectroscopy analysis of thin films obtained at various flow rates. c) Bulk density and electrical conductivity as a function of flow rate.

$$E = \frac{1}{2}C \times V_{bd}^2, \text{ in Joule} \quad (3)$$

2. Results and Discussion

To optimize the properties of the TaN current collector by reactive sputtering, the effect of the nitrogen flow rate in the deposition plasma was first investigated. The deposition time of each layer was tuned to reach 100 nm-thick films (Figure S1, Supporting Information).

The diffractograms for various TaN layers are shown in **Figure 2**a. For the deposition with N_2 = 0% (i.e., in pure argon atmosphere), the three diffraction peaks at 33°, 38°, and 70° can be indexed as the (002), (202), (004) peaks of β-Ta respectively (JCPDS sheet 04-011-3914). With the addition of nitrogen in the plasma (starting from $N_2/(N_2 + Ar)$ = 9%), the diffractogram changes radically: the (002), (202), and (004) peaks corresponding to the β-Ta are retained, but due to preferred orientation effects, (202) peak becomes the most intense. The peak observed at 34.5°, can be indexed to the (110) of the hexagonal TaN (JCPDS sheet 00-039-1485). Finally, the two other peaks at 2θ = 69.6° and 82.5° can be attributed to the (211) and (220) planes of the α polymorph of Ta metal. The appearance of this last phase, following the incorporation of a small amount of N_2 in the plasma has already been reported in the literature.[17,18] Thus, the introduction of N_2 (9%) into the deposition plasma led to the progressive appearance of Tantalum Nitride (TaN). But the layer is composed of 3 phases, namely α and β Ta and hexagonal TaN. Starting from 17%, no trace of peaks corresponding to Ta α nor β can be seen. Despite the broadness of the peaks, i.e., a poorly crystallized layer, the peak at 2θ = 34.5° is attributed to the (110) plane of hexagonal TaN, while the peaks at 35.8° and 41.6° correspond to the (111) and (200) planes of cubic TaN, respectively (JCPDS sheet 00-049-1283). By increasing the fraction of N_2 in the deposition plasma, the (110) peak of hexagonal TaN becomes sharper and shifts toward higher values of 2θ, indicating a decrease in the cell parameter. In the meantime, the peaks corresponding to cubic TaN disappear from 29%. However, given the rather low crystallinity of TaN layers, X-ray diffraction is not the best characterization tool and thus, Raman spectroscopy was carried out to support the XRD

conclusion. The spectra are shown in Figure 2b. From 0% to 9%, no signal can be attributed to Ta-N bonds. From 17% N_2, two peaks appear at 118 ± 5 cm^{-1} and 189 ± 10 cm^{-1}. These peaks have already been observed in the literature and attributed to Ta-N bonds: respectively to the first-order transverse acoustic mode, and the first-order longitudinal acoustic mode.[19] We also note that the peaks become increasingly defined as the N_2 content increases. Raman spectroscopy combined with XRD analyses thus enables to confirmation of the formation of a TaN-containing thin film as soon as the gas ratio is higher than 17%.

Figure 2c shows the evolution of the density and conductivity of deposited thin films versus the $N_2/(N_2+Ar)$ ratio. The conductivity increases when the gas ratio varies from 0% to 9%. This result is consistent with diffraction analyses showing that, in pure argon, the film is composed of β-Ta (conductivity of 6 000 S cm^{-1}), and the introduction of nitrogen in the plasma leads to the formation of various crystalline compounds, including α-Ta, which has much better conductivity than β-Ta, (40 000 S cm^{-1}). Moreover, this behavior has already been reported in the literature.[17,18] When the gas ratio is increased above 9%, conductivity decreases steadily. This is due to the disappearance of the α and β phases of Ta metals, which have both a better conductivity (40 000 and 6 000 S cm^{-1}, respectively) than tantalum nitride (TaN, between 2500 and 4000 S cm^{-1})[18,20] On the other hand, it can be hypothesized that increasing the rate of N_2 in the deposition plasma increases the amount of nitrogen in the layer, leading to the formation of N-rich amorphous phases such as Ta_5N_6 and/or Ta_3N_5 which are less conductive than TaN.[18] Figure 2c also shows the evolution of bulk density (in g cm^{-3}) as a function of gas ratio, which decreases as the rate of N_2 increases. This decrease can be attributed to the transition from dense β-Ta and α-Ta-based phases (16.29 and 16.69 g cm^{-3} respectively) when working at low N_2 rates, to less dense phases when increasing the N_2 rate, such as cubic TaN, hexagonal TaN or Ta_3N_5 (15.84; 14.31; 9.99 g cm^{-3} respectively). For high-power micro-capacitors, the selected TaN layer is the current collector and thus has to be highly conductive. The TaN layer that fulfills such a requirement is the one deposited with a gas ratio close to 23% and will therefore serve as the current collector for TaN/Ta_2O_5 electrode of the electrolytic micro-capacitor.

After the TaN optimization, the tantalum oxide layer is then carefully investigated. The results are reported in **Figure 3**. The deposition time was tuned to deposit 100 nm-thick layers (see Figure S2, Supporting Information). In order to determine the stoichiometry of the deposited layer as a function of the oxygen content, XPS analyses were carried out on Ta_2O_5 films deposited with a gas ratio variation between 10% and 100%. The Ta *4f* and O *1s* core levels spectra are plotted in Figure 3a,b. For both O *1s* and Ta *4f* spectra, we notice a binding energy shift toward higher energy when the O_2 flow rate increases in good agreement with the literature.[21] When we focus on the Ta *4f* spectra of film made with O_2 flow rate close to 10%, we observe 2 additional peaks that are absent on the sputtered films made at a higher O_2 flow rate. These two additional peaks at lower binding energy (22–24 eV) are attributed to the presence of tantalum oxide with an oxidation degree lower than 5, as reported in the literature.[21,22] The contribution of tantalum species in the film was evaluated by XPS. According to the fitting process at the Ta *4f* core level, the film is composed of Ta^{5+} (≈53%), Ta^{3+} (≈30%) and Ta^{+} (≈17%).

Figure 3c shows the evolution of oxygen to tantalum ratio as a function of the gas ratio in the plasma. The sample made at 10% shows a ratio O/Ta of 2, i.e., a TaO_2 stoichiometry. This condition does not satisfy the desired stoichiometry for an electrolytic capacitor based on tantalum compound[8,9] considering Ta_2O_5 (O/Ta = 2.5) is the required dielectric material. When the gas ratio is set between 20% and 100%, the oxygen-to-tantalum ratio ranges between 2.3 and 2.7, close to the expected value of 2.5. Figure 3d shows the density of the layers as a function of the oxygen content determined from the critical angle of the XRR curves. The density of the layer with 10% O_2 is much higher (≈13.2 g cm^{-3}) than that of the pure bulk Ta_2O_5 (≈8.2 g cm^{-3}), indicating the probable presence of high-density species, i.e., Ta metal. For Tantalum oxide layers made between 20% and 100%, the density is systematically lower than that of theoretical Ta_2O_5, coherent with a slightly porous morphology, although cross-section SEM images of the different layers show a compact microstructure (Figure S2, Supporting Information). The density slowly decreases with increasing O_2 content: at 20%, the density is ≈7.2 g cm^{-3} while for the sample made at 100%, the density is lower and close to ≈6.5 g cm^{-3}.

At this stage of the study, it is difficult to clearly select the deposition parameters that allow to production of a good dielectric layer for an electrolytic micro-capacitor operating in an aqueous electrolyte. We thus studied the electrochemical properties of Ta_2O_5 films: various Si/TaN (40 nm)/Ta_2O_5 (40 nm) electrodes were characterized via a 3-electrodes set-up in 0.5 M H_2SO_4 aqueous electrolyte. We performed cyclic voltammetry (CV) characterization by progressively increasing the potential window toward positive potentials until the capacitive behavior of the electrode was lost, i.e., as soon as the CVs could not fit into a rectangular shape profile. CV measurements on the sample made at 10% are shown in Figure S3a (Supporting Information). Strong oxidation currents are observed as soon as the potential exceeds 0.5 V versus Ag/AgCl, and peak intensity decreases progressively as a function of the number of cycles. From these observations, we can assume that the oxidation phenomena originate from the Oxygen Evolution Reaction (OER) resulting in the oxidation of TaO_2 to Ta_2O_5 layers. These electrochemical measurements confirm that a TaO_2 layer is not suitable as a barrier dielectric layer for an electrolytic micro-capacitor. The CV curves for the remaining electrodes are presented in **Figure** 4a,b. Two different behaviors can clearly be observed between the electrode in which the Ta_2O_5 film is made with a gas ratio of 20%, and the other films (50%, 80%, and 100%).

The electrodes coated with Ta_2O_5 films made at various gas ratios (from 50 up to 100%) show a clear oxidation phenomenon between 20 and 24 V versus Ag/AgCl (Figure 4a) whereas the Ta_2O_5 electrode synthesized at 20% maintains an almost rectangular CV curve with a slight oxidation current up to 24 V versus Ag/AgCl (Figure 4a,b). However, it's important to note that for each sample this oxidation current tends to decrease with repeated CVs showing a self-healing effect. The film exhibiting the best barrier property is the one deposited at 20% and we assume the density is an important parameter to avoid contact between the TaN layer and the aqueous electrolyte. As this Ta_2O_5 film exhibits the highest density among all layers deposited at high O_2 rates, the CV is very close to a rectangular shape profile up to 24 V versus Ag/AgCl. Even if it is difficult to unambiguously conclude,

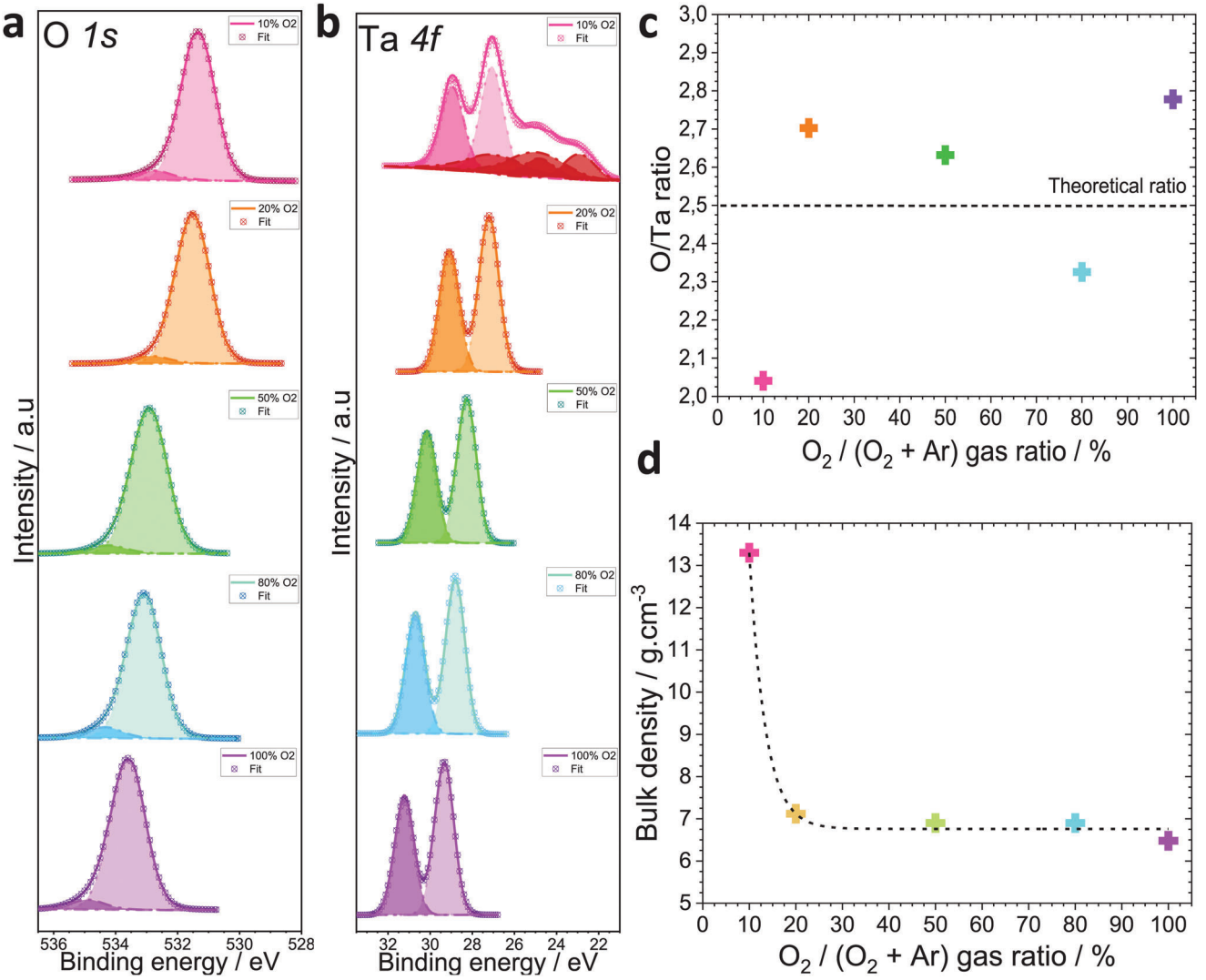

Figure 3. XPS and density analyses of sputtered Ta_2O_5 films. a) XPS analyses at Ta *4f* core level. b) XPS analyses at O *1s* core level. c) Determination of the oxygen to tantalum ratio as a function of the gas ratio in the deposition plasma. d) Density of various Ta_2O_5 films as a function of gas ratio, determined from the evaluation of the critical angle of XRR measurement (see SI).

cross-section SEM images (Figure S2, Supporting Information) show that film made at 20% is denser than the other. Presumably, the high density of the 20% layer, combined with its very compact microstructure, means that the aqueous electrolyte is less likely to diffuse close to the TaN/Ta_2O_5 interface, and thus generate an oxidation current. For this reason, we then afterward decided to study the behavior of various electrodes having a Ta_2O_5 barrier dielectric layer deposited with this optimal gas ratio of 20%.

To evaluate the electrical properties of the optimized 40 nm-thick Ta_2O_5 layer made at 20%, Metal/Insulator/Metal (MIM) devices were fabricated with two different current collectors (Ta or TaN) to give rise to Ta/Ta_2O_5 (40 nm)/Ta or TaN/Ta_2O_5 (40 nm)/TaN stacked layers. Structural analysis of 40 nm-thick Ta made by XRD film is shown in Figure S3b (Supporting Information) and reveals that Ta current collector is, as expected, composed of tetragonal β-Ta. Cross-sectional SEM images of the 2 types of stacked layers and optical top-view images are shown in the inset of Figure 4c. The thicknesses of the individual layers of the two devices (40 ± 5 nm) were evaluated by SEM. To ensure good reliability of the dielectric measurements and their evolution with the area, the size of the metallization pads used for the top electrode was tuned via the lift-off process described in the methods section.

The dielectric constant of the Ta_2O_5 film versus the surface of the top electrode is shown in Figure 4c. Dielectric constant values were determined via impedance measurements by modeling the data with a C_p // R_p equivalent circuit. The C_p values used to calculate the dielectric constant via Equation (1) were taken at 1 kHz. The dielectric constant values are roughly the same for both stacks, i.e., $\epsilon_r = 24.1 \pm 1.5$ for the 1st Ta/Ta_2O_5/Ta MIM device and 24.7 ± 1.6 for the 2nd TaN/Ta_2O_5/TaN system. The values obtained are in good agreement with the dielectric constant values of Ta_2O_5 found in the literature.[23] The evolution

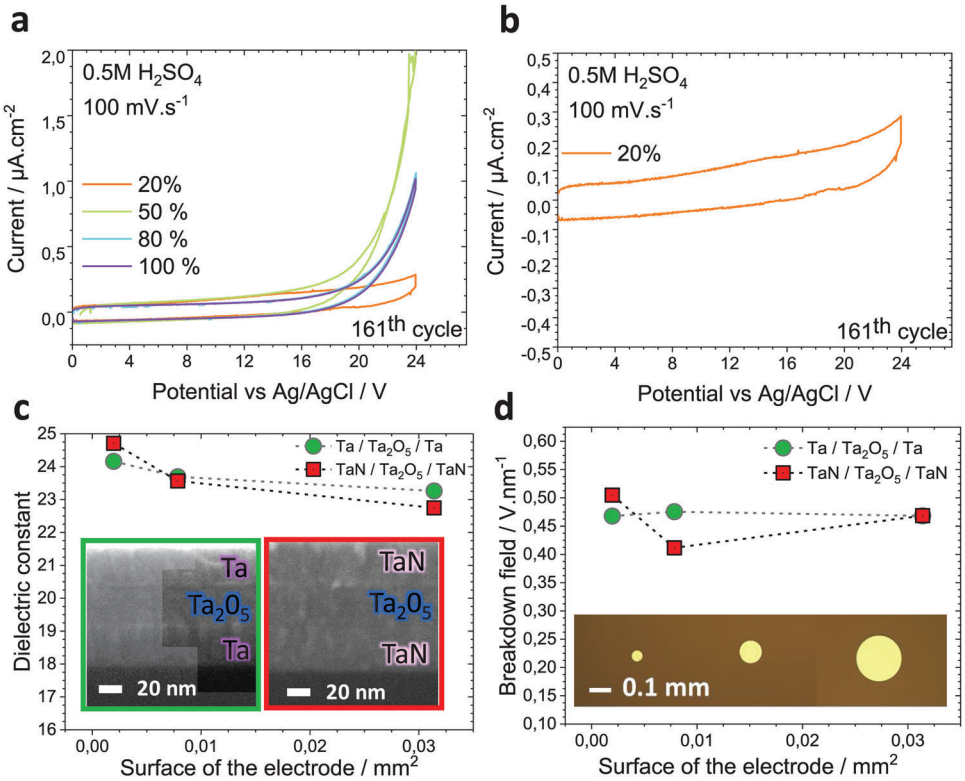

Figure 4. Electrical and Electrochemical characterization of the Ta_2O_5 dielectric layer. a) CV plots of the Si/TaN/Ta_2O_5 electrode deposited at various gas ratios. b) Zoom on the CV plot of the Si/TaN/Ta_2O_5 electrode deposited at 20%. c) Evolution of the dielectric constant versus the surface of the electrodes for the 2 types of MIM devices (Ta/Ta_2O_5/Ta and TaN/Ta_2O_5/TaN). The inset shows the SEM cross-section image of the 2 MIM devices. d) Evolution of the breakdown field of Ta_2O_5 measured in the 2 MIM devices. The inset shows a top-view optical image of the electrode surface.

of the breakdown field as a function of the surface is presented in Figure 4d. For the Ta/Ta_2O_5/Ta stacking, the breakdown field is ≈0.47 ± 0.03 V nm^{-1}, while for the TaN/Ta_2O_5/TaN MIM device, the breakdown field is ≈0.50 ± 0.05 V nm^{-1}. The breakdown field as well as the dielectric constant values between the two stacks are similar in agreement with the value issued from the literature.[23]

As seen from Equations (1) and (2) and Figure 1, to maximize the performance (capacitance and voltage of the electrolytic capacitor), the thickness of the dielectric layer has to be selected as a compromise. Thus, regarding the breakdown field of the Ta_2O_5 film made at 20% (≈0.5 V nm^{-1}), to deliver at least 10 V, the thickness has to be higher than 20 nm. We then set the thickness of the Ta_2O_5 at ≈25 nm, and the theoretical breakdown voltage of the electrolytic micro-capacitor is thus ≈12.5 V. It is crucial to investigate how both current collector-dielectric film and dielectric film-aqueous electrolyte interfaces behave regarding the operating voltage.

Two micro-capacitors made from Ta/Ta_2O_5 and TaN/Ta_2O_5 electrodes were cycled at various positive potentials versus Ag/AgCl. To precisely determine the experimental breakdown voltage of these 2 electrodes, we used the breakdown field measurements determined from the MIM devices, as well as the film thickness accurately determined from the XRR measurement presented in figures S4 and S5 (Supporting Information). The layer thicknesses of the two electrodes are summarized in **Table 1**.

The thicknesses of the Ta/Ta_2O_5 electrode are 44 and 25 nm respectively, while the thicknesses of the TaN/Ta_2O_5 electrode are 43 and 23 nm respectively, so the two stacked layers have similar thicknesses. Therefore, from the breakdown field measurement shown in Figure 4d, we expect a breakdown voltage of 11.8 ± 0.7 V for the Ta/Ta_2O_5 electrode and 11.5 ± 1.2 V for the TaN/Ta_2O_5 electrode.

Based on these experimental breakdown voltages, we thus investigated the evolution of the various interfaces as a function of the applied voltage. The obtained results for the Ta/Ta_2O_5 electrode cycled between 0 and 12, 16 and 20 V versus Ag/AgCl respectively in 0.5 M H_2SO_4 at 20 $mV.s^{-1}$ are summarized in **Figure 5**.

Figure 5a shows the last CV cycle of the Ta/Ta_2O_5 electrode. To avoid irreversible electrode breakdown, the potential window is progressively widened toward positive potential values. The protocol for gradually increasing the potential window is given in Figure S6 (Supporting Information) and described in the method section. A strong oxidation current appears once the theoretical breakdown voltage is exceeded: the maximum current is 50 times more intense for the electrode cycled up to 20 V versus Ag/AgCl

Table 1. Thicknesses of the current collectors and dielectric films.

Electrode	Current collector [nm]	Dielectric barrier [nm]
Ta /Ta_2O_5	44	25
TaN /Ta_2O_5	43	23

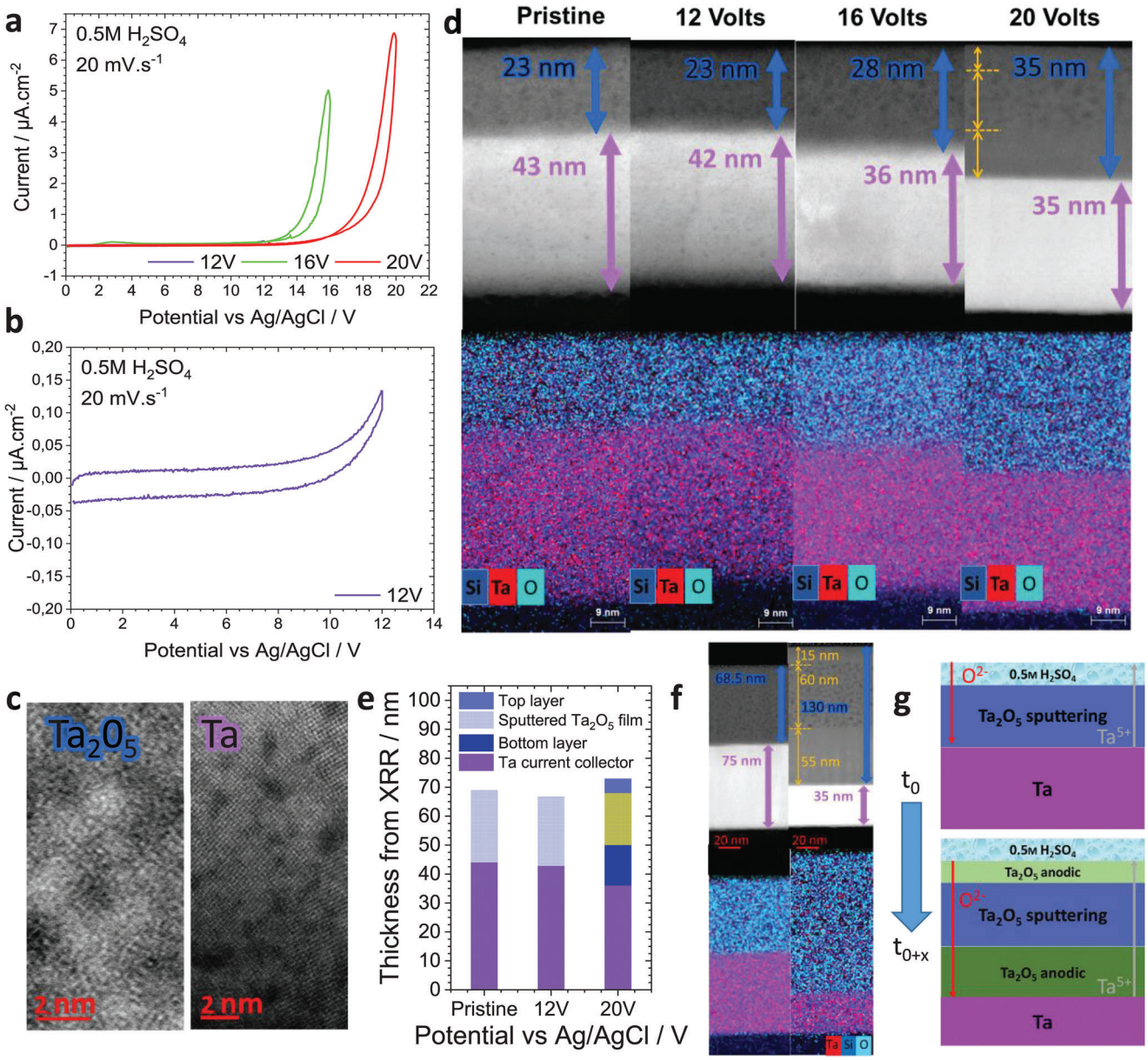

Figure 5. Characterization of the different interfaces in sputtered Ta/Ta_2O_5 electrodes cycled in 0.5 M H_2SO_4 at various upper potentials versus Ag/AgCl. a) CV plots of the Ta/Ta_2O_5 (43/23 nm) electrode cycled in between 0–12, 0–16, and 0–20 V versus Ag/AgCl respectively. b) Zoom on the low current values for the 0–12 V window. c) HAADF STEM image of sputtered Ta_2O_5 and Ta films. d) HAADF STEM image and chemical EDS mapping of the Ta/Ta_2O_5 (43/23 nm) at various potentials versus Ag/AgCl showing the "thickening effect" of the tantalum oxide layer. e) XRR-determined thickness of Ta/Ta_2O_5 electrode as a function of the applied potential window. f) HAADF STEM image of thicker Ta/Ta_2O_5 electrode (75/70 nm) before and after cycling up to 75 V versus Ag/AgCl. g) Schematic diagram of the anodization process taking place in the Ta/Ta_2O_5 electrodes cycled at various potentials in 0.5 M H_2SO_4 aqueous electrolyte.

than the one cycled up to 12 V versus Ag/AgCl. No outgassing was observed in the liquid electrolyte during CV measurements. This suggests that the high oxidation currents are not due to electrolyte degradation via the Oxygen Evolution Reaction (OER) and we can thus conclude that this high oxidation current is due to a modification of interface. Note also that, even if we observe a strong oxidation current (Figure 5a), the electrodes remain functional, i.e., they keep a rectangular CV shape if the potential window is reduced from 0 to 4 V versus Ag/AgCl (see Figure S6, Supporting Information), as expected for capacitive electrode. Additionally, we can observe a decrease of the CV area for the electrode cycling between 0 and 20 V versus Ag/AgCl, indicating a loss of capacitance. From Equation (1), the decrease in the capacitance value is observed to be due to a progressive increase in the thickness of the dielectric layer upon charge/discharge cycling at high voltage corroborating the previous hypothesis of interface modification.

To understand this interface modification, $Si/Ta/Ta_2O_5$ electrode was carefully analyzed by the Transmission Electron Microscopy method by comparing pristine layers with ones cycled

at various potentials (12, 16, and 20 V versus Ag/AgCl respectively). Figure 5c shows two High-Resolution High Angle Annular Dark Field (HR HAADF) STEM images of the Ta_2O_5 and the Ta films in which the intensity is proportional to the atomic number Z. For the both layers, they show black contrast area of ≈2 nm which can be attributed to the presence of porosities. As already pointed out with the XRD analysis (Figure S3b, Supporting Information), the Ta layer is crystallized and shows typical interference fringes in the HR TEM image. HAADF images and chemical composition analysis by EDS elemental mapping of the Ta/Ta_2O_5 electrode are depicted in Figure 5d. When comparing a pristine Ta/Ta_2O_5 electrode (43 / 23 nm) with the 0–12 V cycled one, no noticeable change can be observed. We have to remember that the breakdown voltage of such a 23 nm-thick Ta_2O_5 film is roughly 11.8 Volts, thus for this condition, we probably remain under this threshold value. However, for the electrode cycled between 0 and 16 V versus Ag/AgCl, strong changes can be observed: the thickness of the Ta layer decreases from 43 nm down to 36 nm and, concomitantly, the thickness of the Ta_2O_5 film increases from 23 nm to ≈28 nm. A similar phenomenon is observed when the electrode is cycled up to 20 V versus Ag/AgCl: decreasing the Ta thickness from 43 to 35 nm and increasing the Ta_2O_5 thickness from 23 to ≈35 nm. Focusing on the Ta_2O_5 layer of the 20 V sample, we observe that the tantalum oxide film is actually now composed of three different "sub-layers" with various morphologies (Figure 5d, right images). Starting from the substrate, a first ≈10 nm-thick layer is located at the Ta/Ta_2O_5 interface. The second sub-layer seems to correspond to the one from the pristine electrode (≈23 nm) while the third and last sub-layer (≈3–5 nm-thick) is located at the extreme surface, i.e. at the Ta_2O_5/electrolyte interface. This TEM analysis clearly confirms the thickening of the tantalum oxide layer that was speculated by the decrease of the capacitance observed on the CV measurement. The top surface topology of the electrodes before and after cycling was also characterized by AFM analyses and reported in Figure S7 (Supporting Information). This showed that the roughness of pristine and cycled Ta/Ta_2O_5 electrodes does not vary and stays close to ~ 0.4 nm whatever the applied potential window, despite the formation of the 3–5 nm-thick tantalum oxide sub-layers. To confirm the TEM observations (i.e., at a very local scale, ≈a few nm), we also analyzed the electrodes by XRR, which enables us to probe a macroscopic volume of the sample, while maintaining nanometer accuracy for evaluating the layer thickness. The pristine, "12 V" and "20 V" samples were measured by XRR and then modeled using the Reflex software[15] to determine the thickness of the different layers. The XRR curves with their modeled curves are shown in Figure S4 (Supporting Information) and reported as histograms in Figure 5e. If on the 1 hand, there is very little variation in thickness between the pristine electrode and the sample tested at 12 V, which can be attributed to a small non-uniformity of the layer in the sputtering equipment, on the other hand, for the electrode cycled up to 20 V versus Ag/AgCl, the XRR plot is very different. After modeling the experimental curve, we observe the growth of a 12 nm-thick layer on the top of the sample to reach a total thickness of 36 nm. Note that the thickness of the Ta current collector has decreased from 44 to 37 nm. The thicknesses determined by XRR are in good agreement with those observed by TEM. Hence, the growth of a Ta_2O_5 layer with a morphology more compact than the initial sputtered one is observed when the electrode is cycled beyond the breakdown voltage of the dielectric layer (≈12 Volts), between 0 and 20 V versus Ag/AgCl in the present case. To clarify this "thickening effect" of the tantalum oxide layer, a thicker Ta/Ta_2O_5 electrode (Ta = 75 nm and Ta_2O_5 = 70 nm) was synthesized and submitted to the same electrochemical protocol. To exacerbate the phenomena, the theoretical breakdown voltage of such a 70 nm-thick Ta_2O_5 layer being ≈35 V, we decided to cycle up to 75 V versus Ag/AgCl in 0.5 M H_2SO_4 aqueous electrolyte (Figure 5f). Ta thickness decreased from 75 to 35 nm, while the total thickness of the tantalum oxide layer increased from ≈70 to 130 nm. Similar phenomena occurred at the Ta/Ta_2O_5 and Ta_2O_5/aqueous electrolyte interfaces with the "thickening effect" of the oxide layer resulting from the formation of three tantalum oxide sub-layers (55, 60, and 15 nm-thick from the bottom to the top respectively) and, concomitantly with the decreasing of the tantalum metal's thickness (from 75 to 35 nm) and reduced capacitance value.

Figure 5a–f unveils the modification of the interfaces when an anode of electrolytic micro-capacitor is cycled in an aqueous electrolyte at a potential higher than the breakdown voltage of the dielectric layer. Based on these results, we assume that oxide growth occurs via an anodization mechanism schematically described in Figure 5h.[8] Growth of such a tantalum oxide film by anodization process is mainly controlled by applying a positive potential to a metal immersed in an electrolyte solution. Under the effect of the potential, Ta^{5+} ions will migrate toward the electrolyte to the negative side, while the anions of the aqueous electrolyte (O^{2-}) will migrate toward the positive Ta.

During the ions migration process, Ta^{5+} cations and O^{2-} anions meet at the interfaces to form Ta_2O_5 following this reaction: $2Ta^{5+} + 5O^{2-} \rightarrow Ta_2O_5$

The proportion of each ion participating in the ionic current is characterized by the ion's transport number.[24] The ratio of transport numbers between Ta^{5+} and O^{2-} determines the ratio between the thickness of the oxide layer that grows at the Ta/Ta_2O_5 interface and at the Ta_2O_5/electrolyte interface. As the transport numbers for Ta^{5+} and O^{2-} are 0.24 and 0.76 respectively,[24] 24% of the Ta_2O_5 layer grows at the Ta_2O_5/electrolyte interface and 76% grows at the Ta/Ta_2O_5 interface. Now, looking at the ratio of the thicknesses of the two compact layers observed after cycling at 20 V versus Ag/AgCl for the first set of tests (low thickness of the layers) (Figure 5d), we notice a similar ratio: the Ta_2O_5 top layer at the extreme surface represents 28% of the thickness of Ta_2O_5 grown after cycling, while the Ta_2O_5 under-layer observed at the Ta/Ta_2O_5 interface represents 78% of the total thickness. Similar ratios are obtained for the thicker Ta/Ta_2O_5 electrode shown in Figure 5f. The "thickening effect" observed and the compact morphology of the top and under tantalum oxide layers are therefore due to an anodization phenomenon.

As we observe the formation of a tantalum oxide layer at the Ta/Ta_2O_5 interface when cycling at high voltage, the layer responsible for the decrease of the capacitance value, we thus decided to select another current collector, moving thus from tantalum metal film to tantalum nitride layer. Indeed, transition metal nitrides are known to be more robust against the oxidation process.[25] The results of the study of TaN/Ta_2O_5 electrodes (~ 40/20 nm-thick) cycled in 0.5 M H_2SO_4 at various potentials are depicted in **Figures 6,7**.

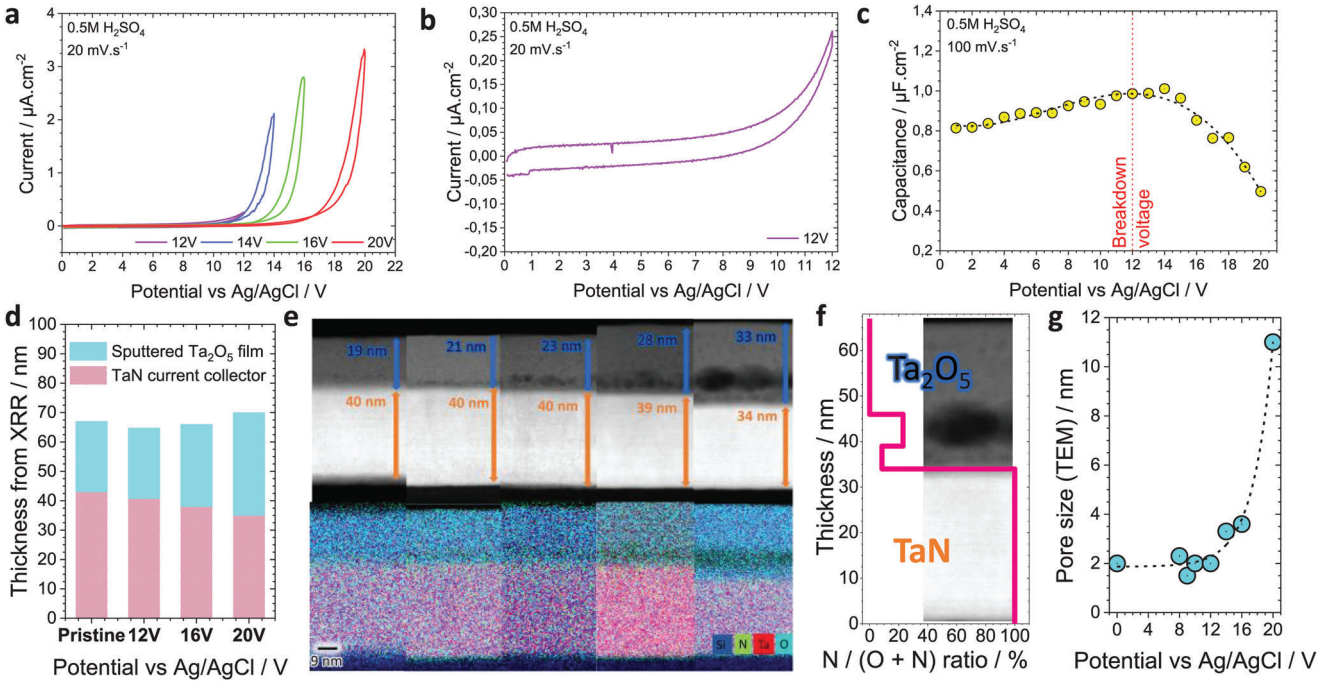

Figure 6. Characterization of the different interfaces in sputtered TaN/Ta_2O_5 electrodes (≈40/20 nm) cycled in 0.5 M H_2SO_4 at various upper potentials versus Ag/AgCl. a-b) CV plots of the TaN/Ta_2O_5 electrode cycled between 0–12, 0–14, 0–16, and 0–20 V versus Ag/AgCl respectively. c) Evolution of the capacitance value as a function of the applied potential. d) XRR-determined thickness of TaN/Ta_2O_5 electrode as a function of the applied potential window. e. HAADF STEM image and chemical EDS mapping of the TaN/Ta_2O_5 at various potentials (12, 14, 16, and 20 V versus Ag/AgCl) showing the "thickening effect" of the tantalum oxide layer as compared to the pristine electrode. f) HAADF STEM image of the TaN/Ta_2O_5 electrode after cycling up to 20 V versus Ag/AgCl and corresponding evolution of the N/(N + O) ratio versus thickness. The porosities (correlated to the black contrast) created at the TaN/Ta_2O_5 interface are clearly highlighted. g) Evolution of the pore size observed at the TaN/Ta_2O_5 interface versus the applied potential.

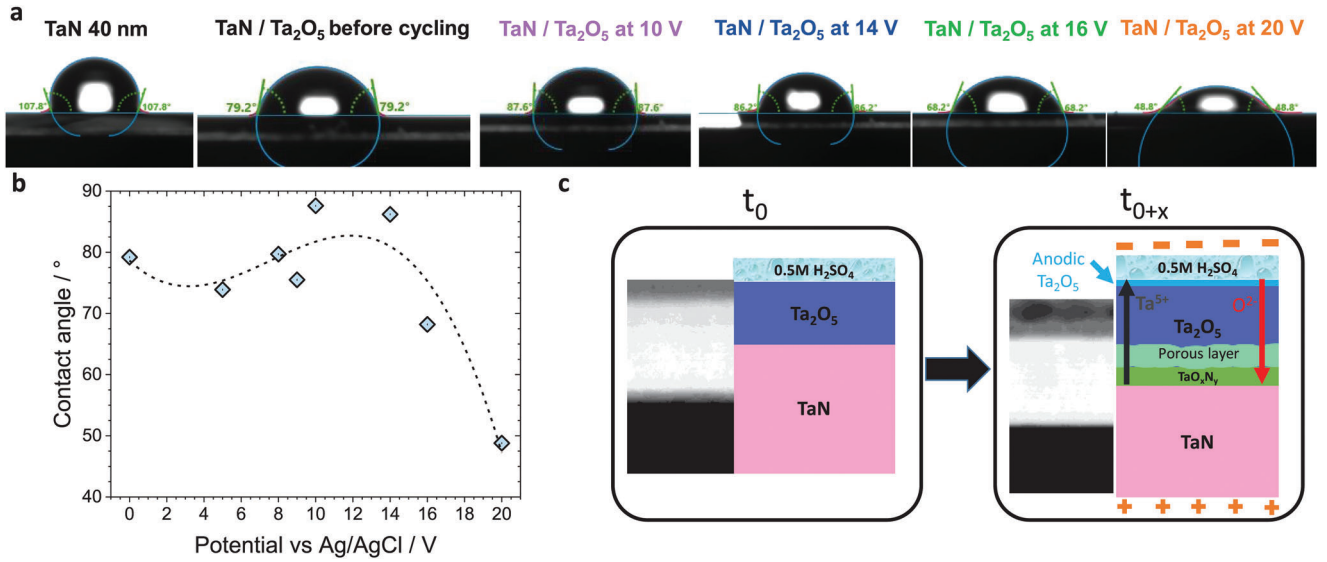

Figure 7. Surface contact angle measurement of the TaN/Ta_2O_5 electrodes cycled in 0.5 M H_2SO_4 at various upper potentials versus Ag/AgCl. a, b) Contact angle measurement of the TaN/Ta_2O_5 electrode cycled in between 0–12, 0–14, 0–16, and 0–20 V versus Ag/AgCl respectively. c) Schematic of the interface modification phenomenon upon cycling above the breakdown voltage of the dielectric layer.

Figure 6a,b depict the CV plots in 0.5 M H_2SO_4 measured at 20 mV s^{-1} between 0 to 12, 14, 16, and 20 V versus Ag/AgCl. As for the Ta metal, once the theoretical breakdown voltage of the 20 nm-thick Ta_2O_5 film is exceeded (11.5 ± 1.2 V), an oxidation current is observed in the graph. However, the maximum oxidation current at 20 V versus Ag/AgCl obtained with the TaN/Ta_2O_5 electrode is twice as low as the one obtained with the Ta/Ta_2O_5 electrode. On the other hand, the capacitance value of the TaN/Ta_2O_5 electrode progressively decreases when cycling up to 20 V versus Ag/AgCl: this decrease was also observed for the Ta/Ta_2O_5 electrode and was attributed to an increase in the tantalum oxide thickness upon cycling. Similarly, despite the high oxidation currents observed during cycling between 0 and 20 V, the electrode remains functional, see (Figure S8, Supporting Information). Figure 6c shows the capacitance of the TaN/Ta_2O_5 electrode (40/20 nm) as a function of the applied potential window. The capacitance was calculated by integrating the current over the capacitive regime of the CVs. The decrease in capacitance once the breakdown voltage (≈12 V) has been exceeded is clearly observed. From these observations, we can assume that the phenomena involved in TaN/Ta_2O_5 are fairly similar to those identified for the Ta/Ta_2O_5 electrode, which we called the "thickening effect" of the tantalum oxide layer. No outgassing was observed in the liquid electrolyte during CV measurements up to 20 V versus Ag/AgCl, as recorded using an optical digital camera (see video supporting files). As previously, to validate our hypothesis, combined XRR and TEM analyses were conducted on the TaN/Ta_2O_5 (≈40/20 nm) electrode to evaluate the thickness of the different layers. The observed and fitted XRR plots can be found in Figure S5 (Supporting Information) and the thicknesses of the different layers were plotted in Figure 6d versus the potential. We observe a decrease in TaN thickness when the electrode is cycled up to 16 and 20 V versus Ag/AgCl moving from 43 nm for the pristine electrode down to 38 and 35 nm, respectively. Concomitantly, the thickness of the oxide layer increased from 23 nm up to 28 nm and 35 nm respectively. Thus, such a finding is again related to an increase in the thickness of the dielectric layer once the breakdown voltage is exceeded as was observed for the Ta/Ta_2O_5 electrode.

As for the previous part, to get information on the morphology before and after cycling, TEM analyses were carried out on FIB lamellae on pristine and cycled samples. Figure 6e shows HAADF TEM images and chemical EDS mapping of the various electrodes. On the one hand, a decrease in the TaN thickness is observed for electrodes cycled above the breakdown voltage, confirmed by the XRR analyses. The thickness of the TaN layer moved from 43 nm to 39 and 34 nm for electrodes cycled up to 16 and 20 V versus Ag/AgCl respectively. On the other hand, an increase in the thickness of the barrier dielectric layer is highlighted moving from 19 up to 33 nm. Additionally, the formation of a compact nanometer-thick layer (≈2.5 nm, Figure S8, Supporting Information) at the electrode/electrolyte interface is observed for the electrode cycled up to 16 V versus Ag/AgCl. For the electrode cycled up to 20 V versus Ag/AgCl, this surface layer was evaluated close to ≈4 nm. These two observations had also been identified for the Ta/Ta_2O_5 electrode. We finally observe the creation of porosity in the oxide layer close to the TaN/Ta_2O_5 interface (Figure 6e,f): the pore size and their distance from the TaN/Ta_2O_5 interface increase as a function of the applied potential. From the chemical mapping images (Figure S9, Supporting Information), it seems that the pores contain nitrogen and oxygen elements. Even if the intensity of the lines emitted by the light elements is thickness-dependent in EDS, it seems reasonable to be able to quantify the N/(N+O) ratio by considering the same thickness. To estimate the N/(N+O) ratio, very local chemical mapping made by STEM-EDS (nanometer probe) was carried out at different locations within TaN/Ta_2O_5 electrode cycled at 20 V versus Ag/AgCl. The results are depicted in Figure 6f and Figure S9 (Supporting Information). This ratio is 100% in the TaN layer and decreases down to 8.5% at the TaN/Ta_2O_5 interface. Within the porosity, localized in the tantalum oxide layer, the ratio increases to 23.7% (there are nitrogen elements detected in the pores) before falling close to 0% in the "bulk" of the Ta_2O_5 layer (very close to the Ta_2O_5/aqueous electrolyte interface). The evolution of pore size as a function of voltage is shown in Figure 6g moving from ≈2 nm up to ≈11 nm for the electrode cycled up to 20 V versus Ag/AgCl.

AFM topology measurements did not reveal any significant change between the pristine electrode and the one cycled up to 20 V versus Ag/AgCl (Figure S10, Supporting Information). Hence, the formation of the nanometer-thick Ta_2O_5 sub-layer at the electrode surface does not alter the roughness. Surface contact angle measurements were carried out to evaluate the wettability of the TaN/Ta_2O_5 electrode against 0.5 M H_2SO_4 aqueous electrolyte. The results are reported in Figure 7a,b. This study showed that the contact angle between the electrode surface and the electrolyte remains close to ≈80° below the breakdown voltage of the tantalum oxide. Once the breakdown voltage has been exceeded, the contact angle decreases to ≈49° due to the nanometer-thick Ta_2O_5 film grown at the electrode surface (anodizing process): the top surface electrode became more hydrophilic toward the acidic electrolyte.

To summarize, we observed a decrease in the TaN thickness and a "thickening effect" of the tantalum oxide layer for TaN/Ta_2O_5 electrodes that have been cycled above the breakdown voltage of the dielectric film. Additionally, when the breakdown voltage is exceeded, we showed the formation of a compact and nanometer-thick Ta_2O_5 layer at the extreme surface of the electrode. The phenomena mentioned above have also been revealed for the Ta/Ta_2O_5 electrode and have been attributed to an anodization mechanism of the Ta layer, as already published.[9,26,27] Nevertheless, the anodization process from TaN layer is very poorly documented in the literature, the only studies showing cases where anodization is carried out from a Ta thin films containing only a fraction of N to form TaN_x, with x <0.33,[28,29] not TaN film. It has however been reported that anodizing a TaN layer leads to the formation of a dielectric layer.[29] This layer is divided into 2 sub-layers: the upper end is composed of Ta_2O_5 and represents 25% of the anodic layer thickness, while the remaining 75% of the layer is composed of TaO_xN_y. Despite the fact we do not know the exact stoichiometry of our TaN_x layer (Figure 2), our observations are in agreement with the literature.[29] Indeed, after cycling the TaN/Ta_2O_5 electrode at high potential, we identified a top tantalum oxide layer at the electrode surface and a bottom TaO_xN_y layer at the TaN/Ta_2O_5 interface. We reported also the formation of porosity in the dielectric layer. This difference is probably due to the increased N concentration in our TaN layer. A tentative explanation is given in Figure 7c summarizing the

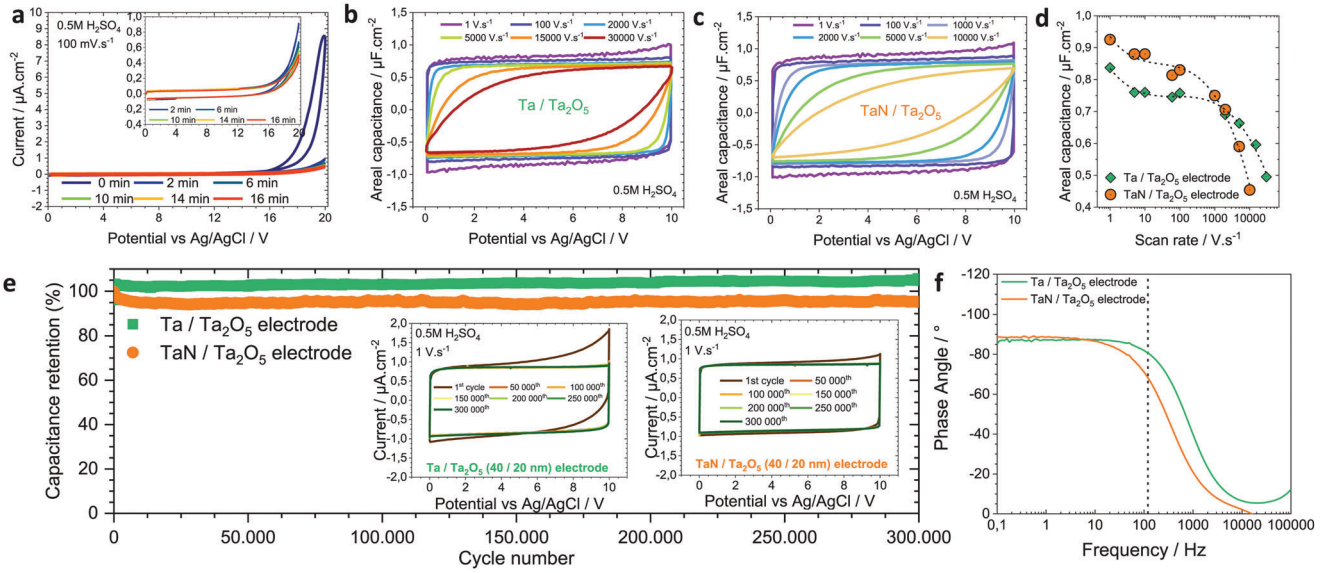

Figure 8. Electrochemical performance of Ta/Ta_2O_5 and TaN/Ta_2O_5 electrodes as an anode from electrolytic micro-capacitor in 0.5 M H_2SO_4. a) Self-healing and thickening effect of TaN/Ta_2O_5 electrode cycled up to 20 V versus Ag/AgCl. b-c) Rate capability performance of Ta/Ta_2O_5 and TaN/Ta_2O_5 electrodes. d) Evolution of the areal capacitance as a function of the scan rate. e. Cycle lifetime of the 2 electrodes during 300 000 cycles at 1 V s^{-1}. f) Frequency performance of the 2 electrodes in 0.5 M H_2SO_4.

involved phenomena when TaN/Ta_2O_5 electrode is cycled at a high potential, i.e., above the breakdown voltage of the dielectric film. The scheme in Figure 7c describes how the electrode is modified starting from t_0, i.e. when the electrode is soaked in 0.5 M H_2SO_4 electrolyte. When the potential is sufficiently high to activate the anodization phenomenon, i.e., at a potential above the breakdown voltage of the Ta_2O_5 film, the process reaches the "$t_0 \pm X$" step and the TaN/Ta_2O_5 electrode initiates its transformation in which the "thickening effect" is highlighted. Under the effect of the electric field, O^{2-} anions coming from the aqueous electrolyte and/or the Ta_2O_5 layer migrate toward the TaN/Ta_2O_5 interface. Simultaneously, Ta^{5+} cations migrate in the opposite direction, toward the Ta_2O_5/electrolyte interface, where they can combine with O^{2-} anions, leading to the growth of an anodic Ta_2O_5 layer at the top Ta_2O_5/electrolyte interface. The O^{2-} ions that would not have reacted at the Ta_2O_5/electrolyte interface will continue their migration until they reach the Ta_2O_5/TaN layer to form a TaO_xN_y layer.

We have shown that the TaN/Ta_2O_5 electrode (≈40/20 nm-thick) cycled up to 20 V versus Ag/AgCl clearly exhibited a high oxidation current. As demonstrated previously, operating at high potential versus Ag/AgCl clearly induced a thickening effect of the Ta_2O_5 layer which could be viewed as a self-healing process. At this step, a question arises: is it possible to obtain a rectangular CV shape over this potential window meaning that we avoid the presence of any oxidation current? To answer this question, we carried out measurement loops consisting of applying a fixed potential close to 20 V versus Ag/AgCl during 120 s and then performing 3 CV at 100 mV s^{-1} from 0 to 20 V versus Ag/AgCl. These results are shown in **Figure** 8a. This loop was performed as many times as necessary until the CVs were identical to each other. It took a cumulative 16 min of polarization at 20 V versus Ag/AgCl to stabilize the CVs. Although the CVs are stabilized, they are not fully rectangular as shown in the inset of Figure 8a but we clearly demonstrate that an electrolytic micro-capacitor made from sputtered TaN current collector and Ta_2O_5 dielectric film is capable of self-healing when operated at potential well above the breakdown voltage of the dielectric layer.

The rate capability of the two types of electrodes was evaluated at various scan rates from 1 V s^{-1} up to 30 000 V s^{-1} for the Ta/Ta_2O_5 and up to 10 000 V s^{-1} for the TaN/Ta_2O_5 electrodes (Figure 8b–d). Half of the initial capacitance value is obtained at the highest scan rate, i.e., at 30 kV s^{-1} for the Ta-based electrode and at 10 kV s^{-1} for the TaN-based electrode (Figure 8d). From these measurements, the ultra-high rate capability of the electrodes is clearly demonstrated as expected from a purely electrostatic charge storage mechanism. Finally, the cycling stability of both electrodes was evaluated between 0 up to 10 V versus Ag/AgCl at 1 V s^{-1} during 300 000 cycles as shown in Figure 8e. After 300 000 cycles, the capacity retention of the two electrodes stays close to ≈100% in good agreement with the one observed for bulk electrolytic capacitors based on tantalum technology,[8] thus validating the proof of the miniaturized concept targeted in this paper. The key parameters of the two electrodes were evaluated by EIS measurements (FigureS11, Supporting Information) and are summarized in **Table 2**. The measured areal capacitance of the two electrodes is ≈0.8 µF cm^{-2} as expected from a planar tantalum oxide-based electrode. Indeed, the theoretical capacitance value of a 23 nm-thick Ta_2O_5 film deposited on a planar

Table 2. Electrochemical performance of the two electrodes.

Electrode	Areal Capacitance at 1 Hz [µF.cm^{-2}]	f_0 [Hz]	τ_0 [ms]
Ta/Ta_2O_5	0,78	830	1,2
TaN/Ta_2O_5	0,82	320	3,2

substrate having a dielectric constant close to 24 is ≈0.9 µF cm^{-2} in good agreement with the measured value. Even if the capacitance value of the electrodes is quite low, it is not the goal of this paper to reach higher performance, since a more fundamental proof of concept of miniaturization is targeted. To reach higher performance and get higher capacitance value at the miniaturized scale, the deposition of Ta, TaN, and Ta_2O_5 films has to be done by Atomic Layer Deposition methods on 3D scaffold having a high area enhancement factor as previously demonstrated in our group for 3D micro-supercapacitors and 3D Li-ion solid-state micro-batteries.[30–36] Note that this 3D micropatterning process leading to the high specific surface electrode is already achieved on bulk electrolytic capacitor during the anodization process of tantalum foil that generates "3D capacitance" of the oxide-based electrode,[8,9] but not at the micro-scale.

Finally, we evaluated the frequency performance of the devices which is a crucial point to transform AC current issued from nano-harvesters to DC current. The magnitude f_0 corresponds to the frequency at which the electrode behaves halfway between a capacitor and a resistor.[37] On the Bode plot, it corresponds to the frequency when the phase angle is equal to –45°. For the Ta/Ta_2O_5 electrode, f_0 is close to 830 Hz while for TaN/Ta_2O_5, it is ≈320 Hz. Since the frequency of the electrical pulses generated by a triboelectric nanogenerator is between a few tens and a few hundreds of Hz, these two electrodes are attractive solutions to combine with the nanogenerator.

Additionally, the time constant, τ_0, represents the time required for the electrode to discharge 50% of its stored energy: for the Ta/Ta_2O_5 and TaN/Ta_2O_5 electrodes, τ_0 are ≈1.2 and 3.2 ms, respectively. These values are in the same order of magnitude as a bulk electrolytic capacitor or as a carbon or graphene MSC.[12]

3. Conclusion and Outlook

Preliminary results for the miniaturization of Ta-based electrolytic capacitor anodes have been demonstrated as a proof of concept. After developing Ta, TaN, and Ta_2O_5 films by magnetron sputtering deposition method, the behavior of Ta/Ta_2O_5 (44/25 nm) and TaN/Ta_2O_5 (43/23 nm) electrodes were studied by electrochemical measurements below and above the breakdown voltage of the Ta_2O_5 dielectric layer. Here we show that cycling at a potential versus Ag/AgCl above the breakdown voltage led to a "thickening effect" of the oxide layer and a change of the electrode morphology as revealed by TEM and XRR analyses. For both electrodes, the thickness of the Ta or TaN current collector decreases if the potential window exceeds the breakdown voltage, while the thickness of the dielectric Ta_2O_5 layer increases. These changes in thickness are accompanied by strong oxidation currents. These observations were attributed to an anodization phenomenon. In contrast, TEM images revealed the presence of a nanoporous layer above the TaN/Ta_2O_5 interface (within the Ta_2O_5 layer) with a pore size distribution of a few nm. These porosities grow as the potential increases above the breakdown voltage. The mechanism leading to the increase in porosity size is not yet understood, and further studies are underway to shed light on this phenomenon. Finally, the two electrodes showed that both have excellent capacity retention over 300 000 cycles. In addition, the characteristic frequency f_0, 830, and 320 Hz respectively for the Ta/Ta_2O_5 and TaN/Ta_2O_5 electrodes would enable these electrodes to be powered by a triboelectric nanogenerator. However, even if the surface capacitance of these electrodes remains quite low (≈0.80 µF cm^{-2}), one way of improving capacity would be to deposit the metal/insulator pair on a 3D substrate with a large specific surface area, thereby increasing surface capacity while maintaining a limited footprint. This would require the use of the Atomic Layer Deposition (ALD) thin-film deposition technique, which has the fundamental property of conformal deposition on 3D scaffold, missing to sputtering technique. However, the deposition of TaN films by ALD seems more feasible than the deposition of Ta metal layer since ALD TaN deposition requires a less severe reducing agent than the ALD Ta deposition.[38–41] To conclude, the TaN/Ta_2O_5 is therefore a very promising electrode for the miniaturization of Electrolytic capacitors technology through 3D scaffolding.

4. Experimental Section

Sputtering Deposition of Ta, TaN, and Ta_2O_5 Thin Films: In this work, Ta and TaN-based (acting as current collectors) and Ta_2O_5 (acting as barrier dielectric layer) were deposited as thin films on a [001]-oriented Si substrate using DC sputtering under vacuum method. All depositions were carried out from a Ta target (Neyco –4″ diameter –99.95%) installed in an Alliance Concept CT200 sputtering cluster deposition tool.

Depositing TaN from the Ta target required working in reactive sputtering mode. We therefore optimized the $N_2/(Ar+N_2)$ gas flow ratio in the deposition plasma, ranging from 9 to 41% N_2 to achieve a thin TaN layer without excessively degrading the electrical conductivity thus keeping the current collector. Other deposition parameters were kept constant, targeting a thickness of 100 nm. The deposition power was set at 300 W (≈3.8 W cm^{-2}), the Ar flow rate at 10 sccm, and the deposition was performed at room temperature.

The Ta_2O_5 deposition by sputtering was also optimized and the effect of the $O_2/(Ar+O_2)$ gas flow ratio in the plasma on the chemical composition of the layer was accurately studied from 10 to 100%. All other deposition parameters were kept constant, targeting a thickness of 100 nm. The pressure was set at 5×10^{-3} mbar, a low value to ensure a dense barrier layer whatever the ratio of O_2 used. Power was set at 150 W (≈1.9 W cm^{-2}), the total flow rate of 20 sccm, and the deposition was done at room temperature.

Structural, Chemical, and Electrical Characterization: For electrical measurement purposes, high resistivity silicon wafers (R > 5000 Ω cm^{-1}) were used and measurements were conducted using the Eddy currents method on a Semilab WT 2000PVN contactless equipment. The morphology and thickness of the films were determined using a Zeiss Ultra 55 Scanning Electron Microscope (SEM) for cross-section analyses. A microbalance from Mettler Toledo XP6U was used to estimate the density of the films (in g cm^{-3}). The following relationship was used to evaluate the bulk density ρ (in g cm^{-3}) of TaN thin film: $\rho = \frac{m}{S \times e}$

Each sample has been weighed before and after deposition to have access to the film weight, m (in g). Then the surface of the sample S (in cm^2) was evaluated by taking a picture of the top surface: the surface value was then deduced from data processing using the *ImageJ* software. The thickness (in cm) has been obtained from SEM cross-section images. The structural properties were studied by X-ray diffraction (XRD), using a Rigaku SmartLab diffractometer in Bragg-Brentano configuration equipped with a Hypix detector, a 9-kW rotating anode, delivering Cu K_α radiation (λ = 1.5418 Å). An offset of 2° relative to the substrate was applied to prevent detector saturation due to the high intensity of the silicon (100) reflection. X-ray reflectometry (XRR) analyses were carried out using the same diffractometer in parallel beam mode, and the data was collected from a $\theta/2\theta$ scan ranging from 0 to 10°. XRR scans were afterward with the fitting software Reflex[15] to extract thicknesses, roughness, and density (through the measure of the critical angle). The Raman

spectra were collected using a LabRAM HR800 Raman spectrometer with an excitation wavelength of 473 nm (HORIBA Scientific, Jobin-Yvon). The X-ray Photoelectron Spectroscopy (XPS) spectra were performed with a 5600 Physical Electronics system and collected from a monochromatic Kα X-ray source (1486.6 eV) and a spherical energy analyzer. After the subtraction of the Shirley-type background, the core-level spectra were decomposed into their components with mixed Gaussian–Lorentzian shape lines using the Multipack software.

Lamellae from both Ta/Ta_2O_5 and TaN/Ta_2O_5 electrodes, required for transmission electron microscopes (TEM) observation, were prepared by the Focused Ion Beam (FIB) technique with a dual-beam Thermo-Fisher Strata DB235 workstation. The high-angle annular dark field (HAADF) images and STEM-EDX (Scanning Transmission Electron Microscopes – Electron Dispersive X-ray spectroscopy) observations of both Ta/Ta_2O_5 and TaN/Ta_2O_5 electrodes extracted by FIB were performed, before and after electrochemical characterization, on a Thermo-Fisher TITAN Themis 80–300 STEM microscope equipped with a high-brightness Schottky field emission gun (X-FEG), a probe aberration corrector for resolution of 0.7 Å in STEM mode, a Super-X quad EDS detector for elemental analysis. The surface morphology of the Ta/Ta_2O_5 as well as the TaN/Ta_2O_5 electrode has been analyzed before and after electrochemical characterization using an Atomic Force Microscope (AFM) Dimension 3100.

The contact angle measurement between the TaN/Ta_2O_5 electrode, after and before electrochemistry characterization, and the solution used as electrolyte purpose for electrochemistry characterization was carried out from a Kruss goniometer DSA 100. The contact angle has been determined from a sessile drop measurement and fitted by the Young-Laplace model.[16]

Fabrication of the MIM Devices: To access the dielectric constant as well as the breakdown voltage of the Ta_2O_5 dielectric layer, 2 Metal-Insulator-Metal (MIM) devices have been processed: Ta/Ta_2O_5/Ta and TaN/Ta_2O_5/TaN. Both devices have been made following the same technological process. First, a metallic (Ta or TaN) layer was deposited on a Si wafer by sputtering deposition method using the recipe previously optimized. A second Ta_2O_5 film was also deposited by the same technique but a small part of the metal layer was partially masked to prevent the deposition of the oxide layer on the total surface. Then, e-beam lithography and a lift-off process allow the depositing of the top electrode metal with various geometric surfaces. To do that, an adhesion promoter HexaMethylDiSilazane (HMDS) was respectively spin-coated, and, EL 13% and PMMA 3% 495K positive e-beam resists. Then, e-beam direct writing creates the top electrode patterns from the designed layout. After the development in a MIBK and IPA solution, the Ta or TaN metal top current collector was afterward sputtered and finally, the sample was soaked in an SVC 14 solution at 70 °C to dissolve the resists to create the MIM devices.

Electrochemical Analyses: The electrochemical measurements, including cyclic voltammetry (CV) and electrochemical impedance spectroscopy (EIS), were performed using a XM Modulab Solartron with a flat cell in a conventional 3-electrode setup in a 0.5 M H_2SO_4 aqueous electrolyte. The sputtered Ta/TaO_5 or TaN/Ta_2O_5 films served as the working electrode, while the reference and the counter electrodes were Ag/AgCl soaked in 3 M KCl solution, and a platinum wire, respectively. EIS spectra were measured by applying a signal amplitude of 20 mV from 1 MHz to 100 mHz at the open-circuit voltage and at different potentials. In order to study the electrode's behavior when the voltage window was extended toward the positive value, a dedicated electrochemical characterization protocol was carried out. It begins with 10 cycles of cyclic voltammetry from 0 to 1 V versus ref at 100 mV s^{-1} then an EIS at 1 V versus ref. Then the positive limit of the potential window by one volt both for the CV and EIS measurements was extended. This protocol as soon as reached the desired potential window was stopped. To study the rate capability of Ta/Ta_2O_5 and TaN/Ta_2O_5 electrodes was carried out CV from 0 to 10 V versus ref at different scan rates. To study the capacitance retention, the Ta/Ta_2O_5 and TaN/Ta_2O_5 electrodes have been characterized by cyclic voltammetry from 0 to 10 V versus ref at 1 V s^{-1} using a VMP3 potentiostat from Biologic.

The surface or areal capacitance (C_S) was calculated from the CV measurements performed under the suitable potential window by normalizing the capacitance measured in microfarad (µF) by the tested area (footprint area in cm^{-2}) of the working electrodes to obtain actual capacitance value in µF cm^{-2}. These metric parameters were calculated according to the following equations:

$$C_S = \frac{\int Idt}{S\Delta V} \tag{4}$$

where I, Δt, S, ΔV, and d are the discharge current (in mA), the discharge time (in s), the footprint area (1.6 cm^2), and the applied potential window (in V), respectively.

Coulombic efficiency (CE) and capacitance retention (C_R) are two other important parameters evaluated from the CV measurements after a long cycling. The coulombic efficiency (defined as the ratio of the measured discharge capacitance to the preceding measured charge capacitance) was usually used to determine the current stability of the electrode, while, capacitance retention was used as a predictor of long-term cycle life. This last indicator was evaluated as the ratio of the measured discharge capacitance of the preceding cycle to the measured discharge capacitance of the previous cycle. CE and CR are expressed in the following equations,[63] respectively:

$$CE = \frac{C_{discharge(n)}}{C_{charge(n)}} \times 100\% \tag{5}$$

$$C_R = \frac{C_{discharge(n+1)}}{C_{discharge(n)}} \times 100\% \tag{6}$$

where charge(n) or discharge(n) (n = 1,2,3, ...) refers to charge/discharge of cycle n.

Supporting Information

Supporting Information is available from the Wiley Online Library or from the author.

Acknowledgements

The authors thank the French National Research Agency (STORE-EX Labex Project ANR-10-LABX-76-01, MEMPACAP ANR project, and PEPR battery (HIPOHYBAT targeted project) program funded by ANR). The French RENATECH network and the University of Lille are greatly acknowledged for supporting the Center of MicroNanoFabrication (CMNF) facility of IEMN. The authors also want to thank the Chevreul Institute (FR 2638) for funding XRD and TEM facilities. X. Wallart and A. Van der Lee are greatly acknowledged for the XPS measurement and the devices used during the XRR fitting process. This work received funding from the CPER Hauts de France project IMITECH and Metropole Européenne de Lille (MEL).

Conflict of Interest

The authors declare no conflict of interest.

Author Contributions

C.T. performed methodology, investigation, formal analysis, and visualization, wrote, reviewed, and edited the original draft, resources, and data curation. J.C. and I.R.-J. performed the development of oxide films. D.T. performed FIB preparation for TEM analyses. M.H. performed formal analysis and investigation (TEM). P.R. performed resources, conceptualization, methodology, and validation, wrote, reviewed, and edited the original draft, supervision, funding acquisition, and project administration. C.L. performed resources, conceptualization, methodology, and validation, wrote, reviewed, and edited the original draft, supervision, funding acquisition, and project administration.

Data Availability Statement

The data that support the findings of this study are available from the corresponding author upon reasonable request.

Keywords

electrolytic capacitor, sputtering, tantalum metal, tantalum nitride, tantalum oxide, thin films

Received: April 29, 2024
Revised: June 21, 2024
Published online:

[1] L. Atzori, A. Iera, G. Morabito, *Comput. Networks* **2010**, *54*, 2787.
[2] A. Whitmore, A. Agarwal, L. Da Xu, *Inf Syst Front* **2015**, *17*, 261.
[3] D. G. S. Pivoto, L. F. F. de Almeida, R. da Rosa Righi, J. J. P. C. Rodrigues, A. B. Lugli, A. M. Alberti, *J. Manuf. Syst.* **2021**, *58*, 176.
[4] P. Song, Z. Ma, J. Ma, L. Yang, J. Wei, Y. Zhao, M. Zhang, F. Yang, X. Wang, *Micromachines* **2020**, *11*.
[5] X. Wu, D.-W. Lee, *Sens. Actuators, A* **2014**, *219*, 73.
[6] C. Wu, A. C. Wang, W. Ding, H. Guo, Z. L. Wang, *Adv. Energy Mater.* **2019**, *9*, 1802906.
[7] C. Lethien, J. L. Bideau, T. Brousse, *Energy Environ. Sci.* **2019**, *12*, 96.
[8] Y. Freeman, *Tantalum and Niobium-Based Capacitors*, Springer International Publishing, Cham **2018**.
[9] J. Both, *IEEE Elect. Insulat. Magaz.* **2016**, *32*, 8.
[10] P. Simon, Y. Gogotsi, *Nature Mater* **2008**, *7*, 845.
[11] F. Wang, X. Wu, X. Yuan, Z. Liu, Y. Zhang, L. Fu, Y. Zhu, Q. Zhou, Y. Wu, W. Huang, *Chem. Soc. Rev.* **2017**, *46*, 6816.
[12] X. Feng, X. Shi, J. Ning, D. Wang, J. Zhang, Y. Hao, Z.-S. Wu, *eScience* **2021**, *1*, 124.
[13] M. Pourbaix, *Atlas of Electrochemical Equilibria in – Aqueous Solutions*, National Association of Corrosion Engineers, **1974**, 644.
[14] G. S. Gudavalli T. P. Dhakal, *Emerging Materials for Energy Conversion and Storage*, Eds. K. Y. Cheong, G. Impellizzeri, M. A. Fraga, Elsevier, **2018**, pp. 247–301.
[15] G. Vignaud, A. Gibaud, *J. Appl. Cryst.* **2019**, *52*, 201.
[16] R. Fitzpatrick, in *Theoretical Fluid Mechanics*, Fitzpatrick, Richard IOP Publishing, Bristol, UK (accessed: December 2017), https://doi.org/10.1088/978-0-7503-1554-8.
[17] K. Min, K. Chun, K. Kim, *J. Vacuum Sci. Technol. B: Microelec. Nanom. Struct. Process.* **1996**, *14*, 3263.
[18] K. Radhakrishnan, N. Geok Ing, R. Gopalakrishnan, *Mater. Sci. Eng., B* **1999**, *57*, 224.
[19] M. Stoehr, C.-S. Shin, I. Petrov, J. E. Greene, *J. Appl. Phys.* **2007**, *101*, 123509.
[20] T. Riekkinen, J. Molarius, T. Laurila, A. Nurmela, I. Suni, J. K. Kivilahti, *Microelectron. Eng.* **2002**, *64*, 289.
[21] T. Tsuchiya, H. Imai, S. Miyoshi, P.-A. Glans, J. Guo, S. Yamaguchi, *Phys. Chem. Chem. Phys.* **2011**, *13*, 17013.
[22] M. T. Brumbach, P. R. Mickel, A. J. Lohn, A. J. Mirabal, M. A. Kalan, J. E. Stevens, M. J. Marinella, *J. Vacuum Sci. Technol. A* **2014**, *32*, 051403.
[23] R. M. Fleming, D. V. Lang, C. D. W. Jones, M. L. Steigerwald, D. W. Murphy, G. B. Alers, Y.-H. Wong, R. B. van Dover, J. R. Kwo, A. M. Sergent, *J. Appl. Phys.* **2000**, *88*, 850.
[24] S. Ono, *Encyclop. Interf. Chem. Surface Sci.Electrochem.* **2017**, 376.
[25] H. Wang, J. Li, K. Li, Y. Lin, J. Chen, L. Gao, V. Nicolosi, X. Xiao, J.-M. Lee, *Chem. Soc. Rev.* **2021**, *50*, 1354.
[26] K. Shimizu, K. Kobayashi, G. E. Thompson, P. Skeldon, G. C. Wood, *Philosoph. Magazine B* **1996**,461.
[27] O. Kerrec, D. Devilliers, H. Groult, M. Chemla, *Electrochim. Acta* **1995**, *40*, 719.
[28] M. Rottersman, R. Pitetti, A. Adolt, M. Bill, *IEEE Trans. Comp., Hybrids, Manufact. Technol.* **1980**, *3*, 500.
[29] S. Dueñas, E. Castán, J. Barbolla, R. R. Kola, P. A. Sullivan, *Solid-State Electron.* **2001**, *45*, 1441.
[30] E. Eustache, P. Tilmant, L. Morgenroth, P. Roussel, G. Patriarche, D. Troadec, N. Rolland, T. Brousse, C. Lethien, *Adv. Energy Mater.* **2014**, *4*, 1301612.
[31] E. Eustache, C. Douard, R. Retoux, C. Lethien, T. Brousse, *Adv. Energy Mater.* **2015**, *5*, 1500680.
[32] M. Létiche, E. Eustache, J. Freixas, A. Demortière, V. De Andrade, L. Morgenroth, P. Tilmant, F. Vaurette, D. Troadec, P. Roussel, T. Brousse, C. Lethien, *Adv. Energy Mater.* **2017**, *7*, 1601402.
[33] E. Eustache, C. Douard, A. Demortière, V. De Andrade, M. Brachet, J. Le Bideau, T. Brousse, C. Lethien, *Adv. Mater. Technol.* **2017**, *2*, 1700126.
[34] B. Bounor, B. Asbani, C. Douard, F. Favier, T. Brousse, C. Lethien, *Energy Storage Mater.* **2021**, *38*, 520.
[35] B. Asbani, G. Buvat, J. Freixas, M. Huvé, D. Troadec, P. Roussel, T. Brousse, C. Lethien, *Energy Storage Mater.* **2021**, *42*, 259.
[36] M. Hallot, V. Nikitin, O. I. Lebedev, R. Retoux, D. Troadec, V. De Andrade, P. Roussel, C. Lethien, *Small* **2022**, *18*, 2107054.
[37] P. L. Taberna, P. Simon, J. F. Fauvarque, *J. Electrochem. Soc.* **2003**, *150*, A292.
[38] H. C. M. Knoops, E. Langereis, M. C. M. Van De Sanden, W. M. M. Kessels, *J. Vac. Sci. Technol., A* **2012**, *30*, 01A101.
[39] O. van der Straten, X. Zhang, C. Penny, J. Maniscalco, S. Chiang, J. Ren, P. Ma, *ECS Trans.* **2013**, *50*, 159.
[40] H. C. M. Knoops, L. Baggetto, E. Langereis, M. C. M. van de Sanden, J. H. Klootwijk, F. Roozeboom, R. A. H. Niessen, P. H. L. Notten, W. M. M. Kessels, *J. Electrochem. Soc.* **2008**, *155*, G287.
[41] H. Kim, C. Cabral, C. Lavoie, S. M. Rossnagel, *J. Vac. Sci. Technol. B* **2002**, *20*, 1321.